Acta Materialia 121 (2016) 78–84

Contents lists available at ScienceDirect

Acta Materialia

journal homepage: www.elsevier.com/locate/actamat

Full length article

Mechanical behavior of copper containing a gas-bubble superlattice

Zhang-Jie Wang [a, b], Frances I. Allen [c, d], Zhi-Wei Shan [b, *], Peter Hosemann [a, **]

[a] Department of Nuclear Engineering, University of California, Berkeley, CA 94720, USA
[b] Center for Advancing Materials Performance from the Nanoscale (CAMP-Nano) & Hysitron Applied Research Center in China (HARCC), State Key Laboratory for Mechanical Behavior of Materials, Xi'an Jiaotong University, Xi'an 710049, China
[c] Department of Materials Science and Engineering, University of California, Berkeley, CA 94720, USA
[d] National Center for Electron Microscopy, Molecular Foundry, Lawrence Berkeley National Laboratory, CA 94720, USA

ARTICLE INFO

Article history:
Received 6 June 2016
Received in revised form
30 August 2016
Accepted 31 August 2016
Available online 13 September 2016

Keywords:
Nanoscale ion implantation
Helium gas-bubble superlattice
In-situ TEM
Ordinary dislocation plasticity
Deformation twinning

ABSTRACT

Helium implantation can cause the formation of a helium gas-bubble superlattice in crystalline materials. Experimental studies of the mechanical response of a material hosting such a superlattice are lacking, especially at the microstructural level. By employing a novel, high-throughput, high-precision nanoscale helium implantation technique, in combination with in-situ transmission electron microscopy nanomechanical testing, we find that the helium-bubble superlattice structure in copper is disordered or maintained depending on whether the material's plasticity occurs by multiple ordinary full dislocations or by deformation twinning. In addition, helium implantation can harden the material significantly: the higher the dose, the larger the yield stress. The measured hardening behavior agrees well with the trend predicted by the Friedel-Kroupa-Hirsch model. Our findings shed new light on understanding the mechanical and microstructural properties of materials subjected to intense helium generation by neutron and alpha-particle bombardment in nuclear fusion, fission or spallation systems.

Materials deployed in nuclear fusion, fission or spallation systems are subject to intense neutron radiation, challenging the system integrity. The neutrons and charged particles generated can cause displacement damage in the system component materials, which may result in the development of larger extended defects such as dislocation loops [1], voids [2], stacking fault tetrahedral (SFT) [3] or even enhanced precipitation and segregation of elements [4]. In addition, neutron-induced nuclear reactions and alpha-particle bombardment can generate large amounts of helium, depending on the neutron energy spectrum and the target material [5]. Typically, if the irradiation dose is high enough or at elevated temperature, then the helium bubbles grow significantly [6,7]. However, if the irradiation temperature is below 35% of the melting temperature of the material, a nano-sized helium gas-bubble superlattice can form [8–11]. Helium gas-bubble superlattices in materials have been studied for decades, but little is known about their behavior under mechanical loading and the effect of an ordered helium-bubble structure on the host material's mechanical properties. Understanding the behavior of gas-bubble superlattices in response to an externally applied stimulus such as a mechanical load is critical for the design of reliable radiation-tolerant structures for clean and safe nuclear energy, in particular nuclear fusion energy. In general, ordinary dislocation plasticity (ODP) and deformation twinning (DT) are known to be responsible for plasticity in metals. However, the question of how ODP and DT interact with a bubble superlattice remains unanswered. Nanotwinned structures have in fact been investigated as a promising irradiation tolerant structure [12–14], thus it is of particular interest to investigate how the bubble superlattice and the dose of implanted helium affect the mechanical behavior of nanotwinned structures.

For fundamental studies of material property changes as a function of helium treatment, helium-ion implantation is often deployed to selectively evaluate the effects of helium content, dose, dose rate and temperature. In the work presented here, we chose copper as a material representative of a large number of face-centered-cubic alloys deployed in nuclear applications due to its well-established structure-property relationships and a large amount of existing data from nanomechanical testing. Focused ion beam (FIB) machining was utilized to fabricate a series of pillars suitable for in-situ transmission electron microscopy (TEM)

* Corresponding author.
** Corresponding author.
E-mail addresses: zwshan@mail.xjtu.edu.cn (Z.-W. Shan), peterh@berkeley.edu (P. Hosemann).

http://dx.doi.org/10.1016/j.actamat.2016.08.085

observation and testing. For the helium irradiation we employed a new implantation technique using a Helium Ion Microscope (HIM) [15] to achieve localized helium implantation to transform fully dense (FD) copper pillars into pillars with a gas-bubble superlattice. Using a nanometer-precise implantation tool such as the HIM enhances sample throughput, repeatability, comparability and precision, since multiple doses can be implanted into individual pillars all manufactured in precisely the same grain. This approach dramatically reduces experimental errors arising from variations in material between samples, or from varying irradiation conditions while increasing the sample throughput dramatically so multiple doses can be investigated in the same experimental run. Hence one can solely focus on the specific variables under study enabling unhindered evaluation of a specific phenomenon. To the best of our knowledge this is the first time the power of the HIM tool has been combined with nanomechanical testing, allowing the design of precise experiments investigating the behavior and influence of helium-bubble superlattice deformation mechanisms (DT or ODP) over a range of implantation doses.

Fig. 1a presents a schematic demonstrating the geometry of the implantation process in which the FIB-fabricated nanopillars are irradiated from opposite sides using a highly localized 25 keV helium ion beam. It is interesting to note that the as-implanted pillars show a rather homogeneous helium bubble distribution along the implantation direction, as shown in the under-focused (−1 μm) bright-field TEM image of a cross-sectioned pillar implanted to 2E17 He ions/cm^2 inset in Fig. 1b. Due to the fact that the helium bubbles are not visible under in-focus (minimum contrast) bright-field TEM conditions, images for defocused conditions (to enhance phase contrast) were acquired. The helium concentration along the implantation direction is estimated from the measured bubble diameter (see detailed diameter measurement in Supplementary Information, Fig. S1) using the equation of state [16–18] assuming all the helium is contained in the bubbles. Following this approach we obtain a helium concentration averaging at around 4 atomic % (Fig. 1b, data points in red; detailed calculation in Supplementary Information, Fig. S3). For comparison, we also estimate the helium concentration for the given implantation dose assuming a nanopillar with a square cross-section (Fig. S2), obtaining a helium concentration of 8 atomic %. Considering that some helium atoms might be lost due to diffusion near the surface, these numbers are in reasonably good agreement. Fig. 1c is the under-focused (−1 μm) bright-field TEM image of the helium gas-bubble superlattice in single-crystal copper aligned along the [110] zone axis. The observations indicate that the bubble arrangement has a two-dimensional periodic character (Fig. 1c), as confirmed by fast Fourier transformation (FFT) of the defocused TEM image (inset in Fig. 1c). Selected area diffraction pattern (SADP) measurements from the entire pillar (Fig. 1d) demonstrate that the helium-bubble superlattice lies in the host copper lattice. For copper pillars with pre-existing twins, the bubble superlattice also exhibits a twin characteristic. A typical example is shown in Fig. 1e (TEM) and 1f (SADP). The green lines in Fig. 1e show the arrangement of helium bubbles along the $(1\bar{1}\bar{1})$ plane on both sides of the $(1\bar{1}1)$ twin boundary (TB) (red line), as confirmed by the corresponding SADP of the copper matrix. In addition, it is found that the TBs do not act as defect sinks for helium, since no significant difference in helium bubble distribution along the TB versus each side is seen (Fig. 1e), in good agreement with the results of a previous study of the influence of a Σ3 TB on the formation of radiation-induced defects [19]. For doses up to 1E18 ions/cm^2, the TBs remained straight and largely unaffected by the helium implantation (Fig. S4), which is different to the case for heavy-ion irradiation experiments performed elsewhere for nanotwinned copper (using Cu^{3+} ions [20], 8.5 dpa) and nanotwinned silver (using Kr^{+} ions [21], 0.6–1 dpa), where both TB migration and roughening were observed. Using the Kinchin-Pease model in the Stopping Range of Ions in Matter (SRIM) simulation software [22], we calculate that the 25 keV helium ions used here produce up to nearly 40 dpa in the pillar implanted with the largest dose of 1E18 ions/cm^2 (Fig. S5). Unlike in the referenced work, in our case no obvious change in the TB is observed. This could be due to the primary knock-on atom spectrum for heavy ions versus helium ions being significantly different. Other more recent codes exist such as Iradina [23] and 3-dimensional Transport of Ions in Matter (3dTRIM) [24] but due to the widespread use of the conventional SRIM we report the data using [22].

In order to reveal the deformation behavior of copper containing a helium-bubble superlattice in response to plastic deformation with ODP as the dominating deformation mechanism, we chose to fabricate and load pillars manufactured in single-crystal copper with the loading direction along the ⟨111⟩ orientation (Fig. 2a). A total of 20 pillars were tested. It was found that compared with FD samples, the bubble-containing samples always exhibited much higher flow stress and smoother plastic flow behavior. In addition, the periodic arrangement of the bubble superlattice was lost after intense plastic strain. A typical example of this phenomenon is shown in Fig. 2 and Movie S1. The corresponding shear stress-strain curve (shear stress given as the normal stress multiplied by the Schmidt factor of 0.2357) is plotted in Fig. 2b (data in red) and gives a critical resolved shear stress (CRSS) for yielding of 350 MPa (denoted by label B in Fig. 2b), with the plastic flow occurring in a rather steady manner. This is in sharp contrast to the FD sample of exactly the same dimensions under the same loading conditions. The CRSS for yielding of the FD sample is only about 141 MPa (denoted by label A in Fig. 2b) and the corresponding plastic deformation exhibits marked serrated characteristics (Fig. 2b, data in black). In-situ TEM observation indicated that ODP played a dominant role in the plastic deformation of the implanted pillar. After the mechanical test, the residual plastic strain reached ~16.7%. Even though the copper matrix of the implanted pillar remained obviously crystalline (as evidenced by the SADP shown inset in Fig. 2c), the periodic arrangement of the helium bubbles was lost (Fig. 2d). This phenomenon can be rationalized by the fact that for a ⟨111⟩ loading direction, six slip systems have equivalent Schmidt factors and therefore multiple slip systems are active. Due to the fact that the helium bubbles interact with several different slip systems and therefore with different Burgers vectors in different directions, the bubbles experience interactions in different directions and lose their ordered structure.

In order to investigate DT deformation in the implanted pillars, a second series of tests with the loading direction along the ⟨200⟩ direction was performed, where deformation by DT is favored [25]. In this case the scenario is significantly different, with both the copper matrix and the bubble superlattice exhibiting twinning. A typical example is shown in Fig. 3, Movie S2. The corresponding shear stress-strain curve (shear stress given by the normal stress multiplied by the Schmidt factor of 0.471) is plotted in Fig. 3b (data in red). The dark-field TEM image of the twinning region after deformation is shown in Fig. 3c and the inset gives the SADP showing the twinning relationship of the crystals, where the yellow and green rectangles show the characteristic parallelogram grids of the matrix and twin diffraction patterns, respectively. The high-magnification under-focused (−1 μm) bright-field TEM image of Fig. 3d clearly shows that the helium-bubble superlattice was maintained after the twinning of the matrix. Upon careful examination it is found that the bubble superlattices on both sides of the twin boundary (red line in Fig. 3d) also exhibit a twin relationship, as evidenced by the FFT of the matrix (Fig. 3e) compared with that of the twin (Fig. 3f). The yellow line in Fig. 3d shows the

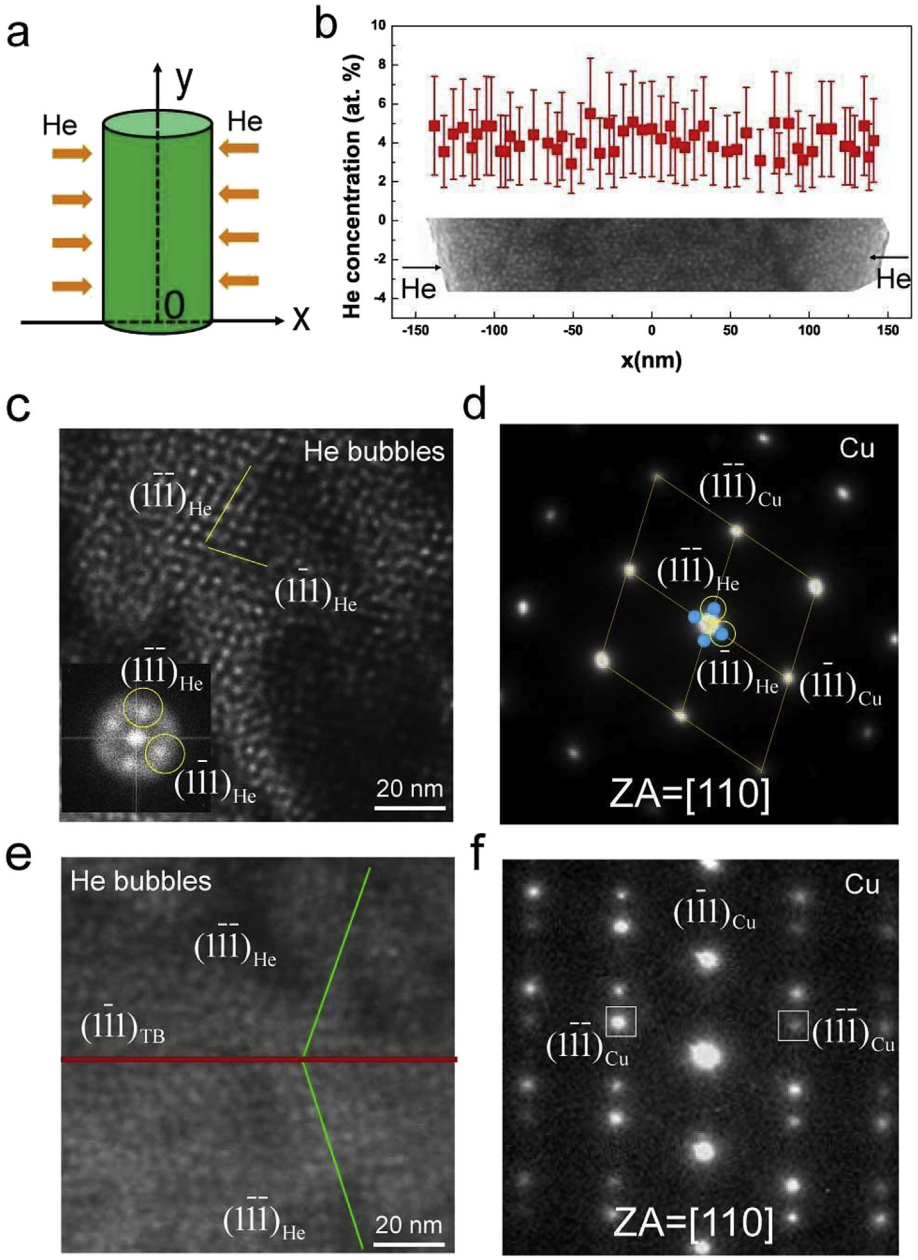

Fig. 1. Nanoscale localized helium-ion implantation and helium gas-bubble superlattice formation in single-crystal copper and nanotwinned copper. (a) Schematic of helium implantation technique. (b) Concentration profile along the implantation direction in the copper nanopillar implanted to a dose of 2E17 He ions/cm^2 (corresponding under-focused (−1 μm) bright-field TEM image of cross-sectioned pillar inset) (c) Under-focused (−1 μm) bright-field TEM image of the helium gas-bubble superlattice in single-crystal copper aligned along the [110] zone axis with FFT inset. (d) FFT spots from the helium gas-bubble superlattice (shown in blue) and SADP of host single-crystal copper lattice from (c). (e) Under-focused (−1 μm) bright-field TEM image of helium gas-bubble superlattice in nanotwinned copper. (f) SADP of nanotwinned copper matrix from (e). (For interpretation of the references to colour in this figure legend, the reader is referred to the web version of this article.)

arrangement of the helium bubbles along the $(1\bar{1}1)_{He}$ plane in the matrix and the green line marks the bubble arrangement along the $(1\bar{1}1)_{He}$ plane in the twin. The two bubble superlattices are symmetrical about the $(1\bar{1}\bar{1})$ twin plane. Thus when the host crystal lattice suffers deformation twinning, so does the helium-bubble superlattice. Fig. 3g shows a schematic illustration of this twinning behavior (see Fig. S6 for a schematic showing the steps of the transformation). Note that during the interaction between the helium bubble and the partial dislocation in the schematic, the bubble is sheared and therefore changes its shape in the process. In our work, bubble deformation was not observed, which could be due to shape recovery by surface diffusion and the energetically favorable shape of a sphere. However, we also note that insufficient spatial resolution of the low-magnification TEM images may also have prevented observation of any bubble deformation. Examination of the TEM movies recorded during the compression testing showed that the nanopillars were in fact first deformed via the motion of ordinary dislocations and were then twinned when the stress reached a certain value. Interestingly, the twins were nucleated early and easily in the implanted pillar (CRSS of 236 MPa denoted by label C in Fig. 3b) compared to the FD sample (CRSS of 377 MPa denoted by label D in Fig. 3b). However, after twin nucleation, twin propagation in the implanted sample was more difficult than in the FD sample, as evidenced by obvious differences in the strain bursts

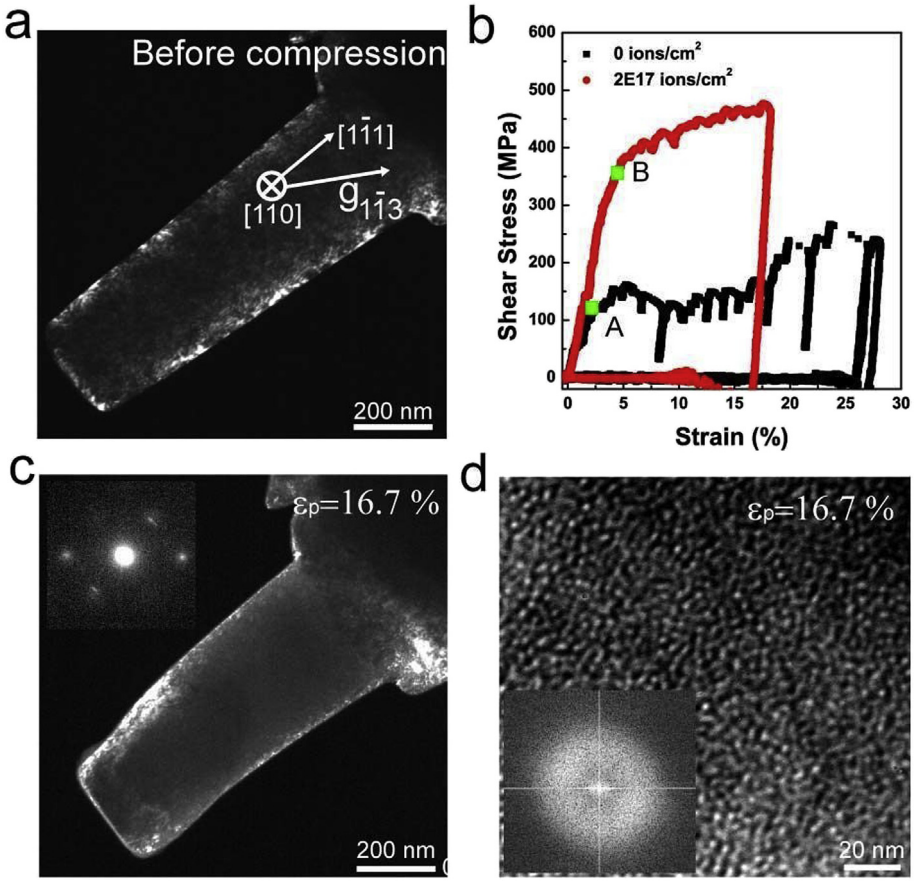

Fig. 2. Disordering of the helium gas-bubble superlattice after ODP by multiple dislocation slip. (a) Dark-field TEM image of ⟨111⟩-orientation copper nanopillar of diameter 250 nm before compression. (b) Engineering shear stress versus engineering strain curves for as-fabricated pillar (black) and pillar implanted with 2E17 He ions/cm^2 (red). (c) Dark-field TEM image of copper pillar after 18% compression strain with SADP inset. (d) Under-focused (−1 μm) bright-field TEM image of helium bubbles in the copper pillar of (c) with FFT of helium bubbles inset. (For interpretation of the references to colour in this figure legend, the reader is referred to the web version of this article.)

seen in the stress-strain curves. In the FD sample, instantaneous strain softening was observed in the form of a large abrupt strain burst. In contrast, twin propagation in the sample containing the bubble superlattice consistently required higher stress.

The enhanced resistance to TB migration in samples containing the helium bubbles will mainly be due to the elastic interaction between the twinning partial dislocations and the helium-bubble superlattice. In order to investigate the effect of the bubble superlattice on TB migration/twinning partial dislocation motion quantitatively, copper pillars containing initial growth twins were fabricated, implanted to different doses (up to 1E18 He ions/cm^2) and subsequently tested by in-situ TEM. Three nanotwinned pillars with the same crystallographic orientation and similar TB densities (insets in Fig. 4a) were FIB-milled from one large grain (see Fig. S7). We find that the flow stress of the implanted nanotwinned copper increases with increasing dose, as shown in Fig. 4a. The slanted TBs inside the three pillars were unstable and migrated in response to the externally applied load (as shown in Movies S3, S4 and S5). The acquisition of the mechanical data and the microstructural evolution following the in-situ TEM approach allowed us to quantify the stress at which TB motion occurs. In other words, the CRSS for TB migration could be measured experimentally. For the as-fabricated non-implanted pillar, and the pillars implanted with 2E17 He ions/cm^2 and 1E18 He ions/cm^2, the CRSS values are 205 ± 23 MPa, 351 ± 40 MPa, and 456 ± 11 MPa, respectively. These values appear in the summary plot of Fig. 4b as solid black circles.

So far, we demonstrated that helium implantation can harden the host material significantly in the dose ranges investigated regardless of the dislocation type (partial or full). Numerous works have focused on helium hardening mechanisms in materials deformed through full dislocations. However, much less investigated is the precise nature of the interaction between helium bubbles and twinning partial dislocations. In the remaining we address this unsolved issue. The barrier strength, defined as $\alpha = \tau_y \lambda / Gb$, has been used to evaluate the strength of the obstacles to dislocation motion, where τ_y is the CRSS for yielding, λ is the average space between obstacles, G is the shear modulus, and b is the Burgers vector of the dislocations. We calculate α to be 0.05 for a full dislocation slip dominated ⟨111⟩ single crystal implanted with 2E17 ions/cm^2 (Fig. 2), and 0.06 and 0.1 for partial dislocation dominated TB migration in nanotwinned pillars implanted to 2E17 ions/cm^2 and 1E18 ions/cm^2, respectively (Fig. 4). The low barrier strengths calculated here indicate that the Friedel-Kroupa-Hirsch (FKH) model may thus be applicable, since this is the model often used to describe the elastic interaction of dislocations with weak obstacles having a defect cluster barrier strength of $\alpha < 0.25$ [26]. The increase in CRSS introduced by the obstacles, $\Delta\tau_{He}$, depends on the helium bubble size and density according to the following relation [26]:

$$\Delta\tau_{He} = \frac{1}{8} GbdN^{2/3} \quad (1)$$

where N and d are the density and diameter of the helium bubbles,

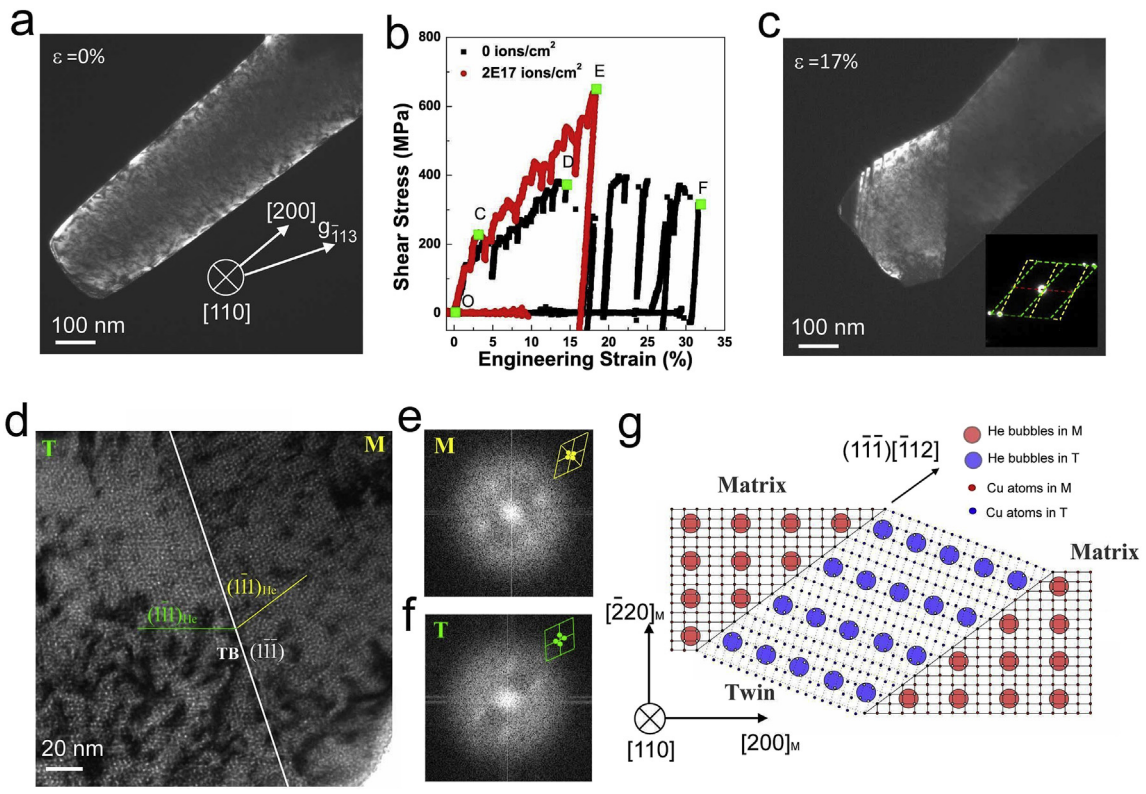

Fig. 3. Twinning-like transformation of helium gas-bubble superlattice after DT. (a) Dark-field TEM image of <100>-orientation copper nanopillar of diameter 210 nm before compression. (b) Engineering shear stress versus engineering strain curves for as-fabricated pillar (black) and pillar implanted with 2E17 He ions/cm^2 (red). (c) Dark-field TEM image of copper pillar after 17% compression strain: DT was observed (SADP inset). (d) Under-focused bright-field TEM image showing symmetrical helium bubble distribution in the matrix and twin. (e) FFT of the region in the twin. (f) FFT of the region in the matrix. (g) Schematic showing the twinning-like transformation of the helium gas-bubble superlattice. (For interpretation of the references to colour in this figure legend, the reader is referred to the web version of this article.)

respectively. The bubble size can be determined from the measured bubble diameter and the corresponding TEM defocus condition [27]. An example is shown in Fig. S1. For the ⟨111⟩-oriented single-crystal copper pillar implanted with 2E17 ions/cm^2 using a beam current of 7 pA (Fig. 2), N is 2.54E25 m^{-3} and d is 1.48 nm. For the nanotwinned copper pillars implanted with 2E17 ions/cm^2 and 1E18 ions/cm^2 using a beam current of 40 pA, N is 2.48E25 m^{-3} and 2.1E25 m^{-3}, and d is 1.37 nm and 2.23 nm, respectively. All the CRSS values calculated using the FKH model are plotted in Fig. 4b (solid green triangle for ⟨111⟩-oriented single-crystal pillar and solid blue triangle for nanotwinned pillar). For the single-crystal and nanotwinned samples implanted to the lower dose of 2E17 ions/cm^2, the experimentally determined values are quite close to those estimated by the FKH model. Thus we conclude that the interactions between the helium gas-bubble superlattice and the full/partial dislocations can both be described well by the FKH model. However, for the higher dose of 1E18 ions/cm^2 in the nanotwinned copper pillar, the FKH model underestimates the CRSS of TB migration (estimate is 365 MPa) when compared with the experimentally measured value (456 ± 11 MPa) (Fig. 4b). We note that all experiments conducted in this work were performed within 1–2 days of the helium implantation, which does raise the question of whether the extremely highly dosed samples reached a steady-state condition. Possibly the helium bubbles become overpressurized resulting in a strengthened material due to the fact that a stronger dislocation/bubble interaction might occur. Alternatively one might speculate that helium remaining in the matrix might cause solid solution hardening. However, given the short distance over which the helium would have to diffuse to reach the next bubble, the second case seems unlikely. In order to verify the above we performed an additional test of two samples two weeks after helium implantation in order to allow enough time for the sample to reach an equilibrium state at room temperature. Interestingly, the strength decreased to the levels estimated by the FKH model (red data in Fig. 4b). Therefore, the mechanical properties measured directly after implantation are representative of a stronger dislocation barrier. The specific reasons for the aging behavior of the material have yet to be understood. However, while the absolute measured stress values change upon aging, the basic observations of strengthening upon implantation are still the same, and furthermore the twinning behavior of the host lattice and bubble superlattice remain unchanged by the aging process.

In summary, we have investigated the fundamental behavior of helium gas-bubble superlattices during deformation twinning and ordinary dislocation plasticity deformations. When the host matrix undergoes deformation twinning, the helium-bubble superlattice itself also exhibits twinning-like transformations as a result of directional intersection of the lattice by twinning partial dislocations. In contrast, the random dislocation motions characteristic of multiple ordinary dislocation plasticity result in a disordering of the periodic arrangement of helium bubbles. Taking advantage of the novel, highly controllable helium implantation technique localized to the nanoscale, we quantitatively studied the dose effect on the mechanical strength and critical resolved shear stress for yield as well as twin boundary motion: the higher the dose, the larger the yield stress and the critical resolved shear stress. We found that helium bubbles induced via high dose-rate implantation are not in full equilibrium with the matrix and aging phenomena can occur. The strengthening induced by equilibrated helium bubbles can be described by the Friedel-Kroupa-Hirsch model, which appears to be

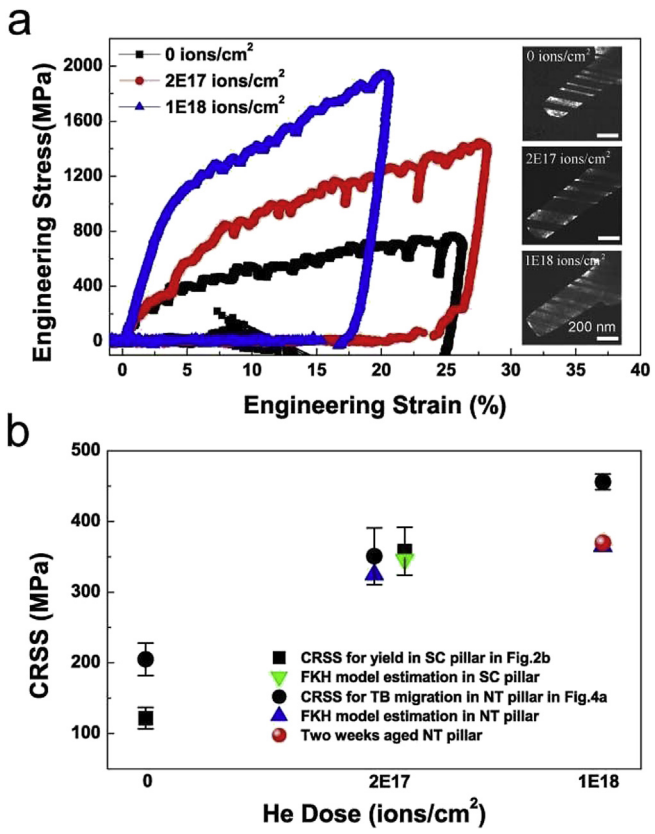

Fig. 4. Increase in TB migration resistance as a result of helium implantation. (a) Engineering normal stress versus engineering strain curves for as-fabricated, 2E17 He ions/cm^2 and 1E18 He ions/cm^2 nanotwinned pillars. The insets are the dark-field TEM images of three copper pillars containing initial growth twins implanted to different doses of helium atoms. (b) Comparison of the experimentally determined and FKH-model calculated CRSS values for ODP in helium-implanted single-crystal (SC) copper pillars and for TB migration in helium-implanted nanotwinned (NT) copper pillars.

applicable to full dislocation motion as well as to twinning partial dislocation interactions.

1. Experimental section

The nanopillars used in this study were all fabricated by FIB milling (FEI Quanta) using 25 keV gallium ions and currents varying from 1.0 nA to 1.6 pA. Two types of nanopillars with different microstructures were studied, single-crystal copper (⟨111⟩-oriented and ⟨001⟩-oriented) and nanotwinned copper. All pillars had a diameter of ~250 nm. The ⟨111⟩-oriented single-crystal pillar was expected to deform by ordinary dislocations and hence enable the study of the helium gas-bubble superlattice in a metal matrix experiencing ordinary dislocation plasticity, whereas the ⟨001⟩-oriented single-crystal pillar was expected to exhibit deformation twinning to enable study of the helium gas-bubble superlattice upon deformation of the metal matrix by twinning. The nanotwinned pillars with slant twin boundaries (TBs) were milled from a polycrystalline nanotwinned copper foil, which was synthesized by means of pulsed electrodeposition. A thin region with a thickness of several micrometers was obtained by mechanical polishing followed by chemical polishing in a solution of methanol with 5 vol.% (vol/vol) nitric acid. The copper nanopillars containing slant TBs were then fabricated in this thinned region.

Nanoscale localized helium implantation was performed using a Zeiss ORION NanoFab Helium Ion Microscope. In the present work, single-crystal copper nanopillars were implanted with 2E17 ions/cm^2 at 25 keV using a beam current of 7 pA. The nanotwinned copper pillars were implanted with 2E17 ions/cm^2 and 1E18 ions/cm^2 using 25 keV helium ions at a current of 40 pA. The pixel dwell time for all implantation scans was set to 10 μs and the pixel (x, y) scan spacings were fixed at 7.69 nm (the nominal probe size is 0.5 nm). Subsequent in-situ TEM compression testing was carried out inside a JEOL 3010 TEM using a Hysitron PicoIndenter (PI95) in displacement-control mode. The loading rate was set to 5 nm/s. The corresponding strain rate was calculated to be around 10^{-3} s^{-1}. The evolution of microstructures during deformation was recorded using a Gatan833 (SC200) CCD camera.

Acknowledgements

The Authors thank The China Scholarship Council for providing funding for Z.W.'s stay at the University of California, Berkeley. This publication was made possible in part by NSF/DMR MRI1338139. The research was performed using funding received from the DOE Office of Nuclear Energy's Nuclear Energy University Programs and the Keck Foundation. Z.S. and Z.W. acknowledge support from the Natural Science Foundation of China (51231005, 51401159, 11132006 and 51321003). We thank Lei Lu's group (Institute of Metal Research, Chinese Academy of Science) for supplying nanotwinned copper samples. The samples were FIB-milled and helium-implanted at the Biomolecular Nanotechnology Center/QB3 at UC Berkeley. The TEM in-situ analysis was performed at The Molecular Foundry, which is supported by the Office of Science, Office of Basic Energy Sciences, of the U.S. Department of Energy under Contract No. DE-AC02-05CH11231. The Authors thank Daryl Chrzan and Ian Stewart Winter (University of California, Berkeley) for useful discussions.

Appendix A. Supplementary data

Supplementary data related to this article can be found at http://dx.doi.org/10.1016/j.actamat.2016.08.085.

References

[1] B. Larson, F. Young, X-ray diffuse scattering study of irradiation induced dislocation loops in copper, Phys. Status Solidi (a) 104 (1987) 273–286.
[2] D.-G. Xie, Z.-J. Wang, J. Sun, J. Li, E. Ma, Z.-W. Shan, In situ study of the initiation of hydrogen bubbles at the aluminium metal/oxide interface, Nat. Mater. 14 (2015) 899–903.
[3] D. Kiener, P. Hosemann, S. Maloy, A. Minor, In situ nanocompression testing of irradiated copper, Nat. Mater. 10 (2011) 608–613.
[4] R. Carter, N. Soneda, K. Dohi, J. Hyde, C. English, W. Server, Microstructural characterization of irradiation-induced Cu-enriched clusters in reactor pressure vessel steels, J. Nucl. Mater. 298 (2001) 211–224.
[5] S.J. Zinkle, L.L. Snead, Designing radiation resistance in materials for fusion energy*, Ann. Rev. Mater. Res. 44 (2014) 241–267.
[6] W. Han, M. Demkowicz, E. Fu, Y. Wang, A. Misra, Effect of grain boundary character on sink efficiency, Acta Mater. 60 (2012) 6341–6351.
[7] M.S. Ding, J.P. Du, L. Wan, S. Ogata, L. Tian, E. Ma, W.Z. Han, J. Li, Z.W. Shan, Radiation-induced helium nanobubbles enhance ductility in submicron-sized single-crystalline copper, Nano Lett. 16 (7) (2016) 4118–4124.
[8] S. Das, M. Kaminsky, Radiation blistering of polycrystalline niobium by helium-ion implantation, J. Appl. Phys. 44 (1973) 25–31.
[9] P. Johnson, D. Mazey, Helium gas bubble lattices in face-centred-cubic metals, Nature 276 (1978) 595–596.
[10] P. Johnson, D. Mazey, Helium gas-bubble superlattice in copper and nickel, Nature 281 (1979) 359–360.
[11] P. Johnson, A. Malcolm, D. Mazey, Importance of stress in bubble ordering in the helium gas-bubble superlattice in copper, Nature 329 (1987) 316–318.
[12] D. Beck, A new interatomic potential function for helium, Mol. Phys. 14 (1968) 311–315.
[13] K. Yu, D. Bufford, C. Sun, Y. Liu, H. Wang, M. Kirk, M. Li, X. Zhang, Removal of stacking-fault tetrahedra by twin boundaries in nanotwinned metals, Nat. Commun. 4 (2013) 1377.
[14] Y. Chen, K.Y. Yu, Y. Liu, S. Shao, H. Wang, M. Kirk, J. Wang, X. Zhang, Damage-tolerant nanotwinned metals with nanovoids under radiation environments,

Nat. Commun. 6 (2015).
[15] B. Ward, J.A. Notte, N. Economou, Helium ion microscope: a new tool for nanoscale microscopy and metrology, J. Vac. Sci. Technol. B 24 (2006) 2871–2874.
[16] Q. Guo, P. Landau, P. Hosemann, Y.Q. Wang, J.R. Greer, Helium implantation effects on the compressive response of Cu nanopillars, Small 9 (2013) 691–696.
[17] R. Mills, D. Liebenberg, J. Bronson, Equation of state and melting properties of He 4 from measurements to 20 kbar, Phys. Rev. B 21 (1980) 5137.
[18] N. Li, M. Nastasi, A. Misra, Defect structures and hardening mechanisms in high dose helium ion implanted Cu and Cu/Nb multilayer thin films, Int. J. Plast. 32 (2012) 1–16.
[19] M.J. Demkowicz, O. Anderoglu, X. Zhang, A. Misra, The influence of $\sum 3$ twin boundaries on the formation of radiation-induced defect clusters in nano-twinned Cu, J. Mater. Res. 26 (2011) 1666–1675.
[20] N. Li, J. Wang, Y. Wang, Y. Serruys, M. Nastasi, A. Misra, Incoherent twin boundary migration induced by ion irradiation in Cu, J. Appl. Phys. 113 (2013) 023508.
[21] J. Li, K. Yu, Y. Chen, M. Song, H. Wang, M. Kirk, M. Li, X. Zhang, In situ study of defect migration kinetics and self-healing of twin boundaries in heavy ion irradiated nanotwinned metals, Nano Lett. 15 (5) (2015) 2922–2927.
[22] J.F. Ziegler, M.D. Ziegler, J.P. Biersack, SRIM–The stopping and range of ions in matter (2010), Nucl. Instrum. Methods Phys. Res. Sect. B Beam Interact. Mater. Atoms 268 (2010) 1818–1823.
[23] C. Borschel, C. Ronning, Ion beam irradiation of nanostructures – a 3D Monte Carlo simulation code, Nucl. Instrum. Methods Phys. Res. 269 (2011) 2133–2138.
[24] C. Borschel, R. Niepelt, S. Geburt, C. Gutsche, I. Regolin, W. Prost, F.J. Tegude, D. Stichtenoth, D. Schwen, C. Ronning, Alignment of semiconductor nanowires using ion beams, Small 5 (2009) 2576–2580.
[25] H.S. Park, K. Gall, J.A. Zimmerman, Deformation of FCC nanowires by twinning and slip, J. Mech. Phys. Solids 54 (2006) 1862–1881.
[26] S.J. Zinkle, Y. Matsukawa, Observation and analysis of defect cluster production and interactions with dislocations, J. Nucl. Mater. 329 (2004) 88–96.
[27] Q. Wei, N. Li, N. Mara, M. Nastasi, A. Misra, Suppression of irradiation hardening in nanoscale V/Ag multilayers, Acta Mater. 59 (2011) 6331–6340.